# Coronene derivatives for transparent organic photovoltaics through inverse materials design†

Jeni C. Sorli,[a] Pascal Friederich,[b] Benjamin Sanchez Lengeling,[b] Nicholas C. Davy,[a] Guy Olivier Ngongang Ndjawa,[a] Hannah L. Smith,[c] Xin Lin,[c] Steven A. Lopez,[d] Melissa L. Ball,[ah] Antoine Kahn,[c] Alán Aspuru Guzik[befg] and Yueh Lin Loo*[ah]

To accelerate materials discovery, computational methods such as inverse materials design have been proposed to predict the properties of target compounds of interest for specific applications. This *in silico* process can be used to guide subsequent synthesis and characterization. Inverse design is especially relevant for the field of organic molecules, for which there are nearly infinite synthetic modifications possible. With a target application of UV-absorbing, visibly transparent solar cells in mind, we calculated the orbital and transition energies of over 360 possible coronene derivatives. Our screening, or the constraints we imposed on the calculated series, resulted in the selection of three new derivatives, namely contorted pentabenzocoronene (cPBC), contorted tetrabenzocoronene (cTBC), and contorted tetrabenzofuranylbenzocoronene (cTBFBC) for synthesis and characterization. Our materials characterization found agreement between our calculated and experimental energy values, and through testing of these materials in organic photovoltaic (OPV) devices, we fabricated solar cells with an open-circuit voltage of 1.84 V and an average visible transparency of 88% of the active layer; both quantities exceed previous records for visibly transparent coronene-based solar cells. This work highlights the promise of inverse materials design for future materials discovery, as well as improvements to an exciting application of UV-targeted solar cells.

## Introduction

The ability to design organic semiconductors with prescribed optoelectronic properties is a primary motivation for their continued exploration and use in organic electronics.[1] This bottom-up tunability enables synthesis of organic semiconductors, whose emission is narrow and wavelength selective[2–5] for organic light-emitting diodes (OLEDs), those that result in mechanically flexible films to be incorporated in organic field-effect transistors (OFETs) on plastic substrates,[6–9] and those that absorb specific ranges of light, including the UV and near-IR, for organic photovoltaics (OPVs).[10–13] While this tunability is advantageous for future materials discovery, it can readily become overwhelming in its vastness, as there are nearly infinite molecular designs to consider.

To more rapidly screen a wide range of molecular designs prior to dedicating efforts towards their synthesis and characterization, the community has leveraged computational power for prediction and data analysis, allowing for more rapid iteration and optimization of materials with targeted properties.[14–20] Consortia, such as the Materials Genome Initiative (MGI)[18,21] or the Harvard Clean Energy Project (CEP),[22] have been established and researchers are actively pursuing methods of exploring and optimizing new organic semiconductors using concepts such as inverse materials design.[15,23,24] While this approach is of great interest to optimize materials discovery, and there are many theoretical efforts predicting compounds of interest, studies in which calculations that target an application and are then followed up with and corroborated by experiments are more limited.[25–28]

[a] *Department of Chemical and Biological Engineering, Princeton University, Princeton, NJ, 08544, USA. E mail: lloo@princeton.edu*
[b] *Chemical Physics Theory Group, Department of Chemistry, University of Toronto, Toronto, Ontario, M5S 3H6, Canada*
[c] *Department of Electrical Engineering, Princeton University, Princeton, NJ, 08544, USA*
[d] *Department of Chemistry and Chemical Biology, Northeastern University, Boston, MA, 02120, USA*
[e] *Department of Computer Science, University of Toronto, Ontario, M5T 3A1, Canada*
[f] *Lebovic Fellow, Canadian Institute for Advanced Research, Ontario, M5G 1M1, Canada*
[g] *Vector Institute for Artificial Intelligence, Ontario, M5G 1M1, Canada*
[h] *Andlinger Center for Energy and the Environment, Princeton University, Princeton, NJ, 08544, USA*

† Electronic supplementary information (ESI) available. CCDC 2040902 and 2040903.

One emerging target application is visibly transparent organic solar cells that absorb ultraviolet (UV) wavelengths.[29] For this specific application, both the donor and acceptor compounds of the organic heterojunction that make up the solar cell active layer must individually have wide band gaps in excess of 2.9 eV to solely absorb UV light and transmit visible light. The use of donor and acceptor materials with wide band gaps can result in solar cells with a high open-circuit voltage ($V_{OC}$), provided that the highest occupied molecular orbital (HOMO) of the donor and the lowest occupied molecular orbital (LUMO) of the acceptor are situated far from each other while also maintaining the required HOMO–HOMO and LUMO–LUMO offsets for exciton dissociation.[30] In order to work towards the design of a transparent OPV, predicting the HOMO and LUMO energy levels of potential organic semiconductor constituents would allow for identification of promising donor–acceptor (DA) pairs for inclusion into the active layer. Density Functional Theory (DFT) is commonly used to predict the HOMO and LUMO energy levels of organic semiconductors[25] for applications in organic photovoltaics.[31–35]

Here, we employed the principles of inverse materials design to identify coronene-based, UV-absorbing compounds for inclusion as active layers in transparent solar cells.[36] Contorted hexabenzocoronene (cHBC) and its derivatives[12,13,37–43] are easily modified to create a library of molecules with a range of frontier orbital energies.[44–46] Generally, coronene derivatives are composed of a coronene core flanked by peripheral substituents, denoted in blue and orange, respectively, in Fig. 1. We identified 362 coronene derivatives as potential candidate chromophores, and calculated their molecular orbital (MO) and excited-state energies using DFT. By imposing constraints specific to our end application, we selected three new coronene-based donor compounds for synthesis and characterization (Fig. 1), including contorted pentabenzocoronene, cPBC; contorted tetrabenzofuranylbenzocoronene, cTBFBC; and contorted tetrabenzocoronene, cTBC. To verify our procedure experimentally, we also made solar cells using these new materials as donors in the active layer, pairing them with chlorinated contorted hexabenzocoronene derivatives previously developed in our group as acceptors,[29,45] the molecular structures of which are shown in Fig. S1 (ESI†). OPVs that incorporate these three new donors exhibit higher transparency and/or $V_{OC}$s than any of those comprising previously reported coronene derivatives.[29] Our top performing solar cell uses cTBC paired with a chlorinated cHBC (4Cl-cHBC) as the active layer; this solar cell exhibits a $V_{OC}$ of 1.84 V and an active layer average visible transmittance (AVT) of 87.5%. This result highlights the utility of *in silico* screening in order to narrow down the selection from a wide range of possible molecule candidates when both a target application and appropriate properties are specified.

## Results and discussion

Coronene compounds are readily derivatized through a four-fold addition of an aryl group appended boronic ester/acid to a benzoquinone derivative *via* a Suzuki cross-coupling reaction that is further ring closed either through a Scholl reaction or Mallory oxidative photocyclization.[47] Given the modularity of this synthesis scheme, outlined in ESI,† and the large libraries of benzoquinone derivatives and boronic esters/acids available, we could theoretically access a large number of coronene derivatives with varying chemical functionalities and electronic properties. This study focused on twelve benzoquinone-derivatives and sixty boronic ester compounds (Fig. S2, ESI†), resulting in a library of 362 possible unique coronene-based compounds as inputs for the screening process. Here, the theoretical and experimental efforts focused on the development of donor compounds, as several halogenated coronene derivatives have been reported[45] and successfully employed as acceptors in coronene-based donor–acceptor pairs.[29,45,48]

The screening process involved five sequential steps: (1) the HOMO and LUMO and excited-state energies were first calculated for each of the 362 possible coronene-based candidate compounds through time-dependent density functional theory (TD-DFT). (2) Once the frontier orbital energies were identified, any individual candidate coronene derivative with a HOMO–LUMO gap, or band gap, less than 2.9 eV was eliminated from the data set. (3) Molecules with $S_1 \rightarrow T_1$ splitting energies less than 0.5 eV were subsequently eliminated. (4) Candidate molecules of

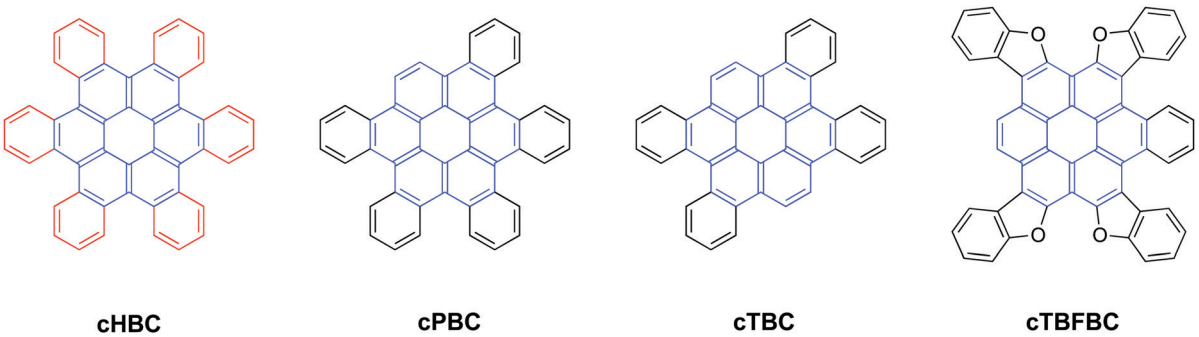


Fig. 1 Overview of coronene derivatives and molecules selected for synthesis and characterization. Highlight of coronene ''core'', shown in blue, and peripheral substituents, shown in orange, on contorted hexabenzocoronene (cHBC). New donor materials include contorted pentabenzocoronene (cPBC), contorted tetrabenzocoronene (cTBC) and contorted tetrabenzofuranylbenzocoronene (cTBFBC).

the reduced pool were paired as potential donor–acceptor (DA) pairs. (5) Any DA pair with a photovoltaic gap, the energy difference between the donor's HOMO and acceptor's LUMO, less than 2.3 eV was eliminated.

The first three steps were straightforward. Materials used as the active layer for a transparent solar cell must not absorb appreciable visible light (with an energy lower than 2.9 eV) for our specified application. We thus needed to identify the frontier orbital energies and then remove any candidate coronene derivatives that had a HOMO–LUMO gap that is smaller than 2.9 eV. Using B3-LYP/SVP level of theory,[22] TD-DFT calculations were performed on the 362 candidate molecules to identify the excited state and frontier orbital energies. The ESI† provides further details on both geometry optimization and the DFT calculations. Calculated HOMO and LUMO energy levels for all possible coronene derivatives are shown in Fig. 2a, and their excited state transition energies are shown in Fig. 2b. We chose to select for molecules with HOMO–LUMO gaps, $E_G$, greater than 2.9 eV to target molecules that absorb exclusively in the UV, shown in Fig. 3a. This criterion narrowed the available library to 211 compounds. Following this decision, we chose to select for molecules with larger triplet splitting energies relative to the spread of the data set, in order to target compounds with a lower probability of exciton transfer from their singlet states to their triplet states. As stated for the Fermi–Golden rule,[49] the rate of intersystem crossing (ISC) is related to the $S_1 \rightarrow T_1$ transition energy difference through a Gaussian functional form, such that as the energy difference increases, the rate of ISC decreases. Previous work has shown decreased rates of intersystem crossing when the singlet–triplet splitting energy is greater than 0.5 eV.[50] We therefore selected a cutoff value of 0.5 eV, as shown in Fig. 3b, to ideally access materials with lower rates of intersystem crossing. This decision further narrowed the candidate molecule pool by approximately 50% to 102 molecules.

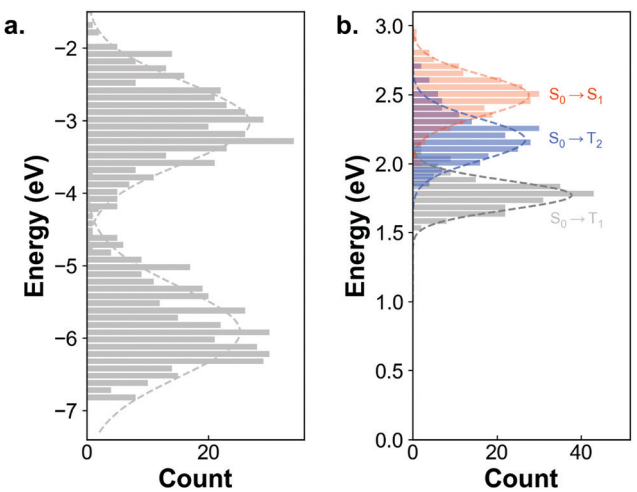


Fig. 2 Calculated values for molecules with different pairings of back bone and substituent fragments. (a) DFT calculated HOMO and LUMO energy levels. (b) DFT calculated transition energy of the $S_0$ $S_1$, $S_0$ $T_1$ and $S_0$ $T_2$ transitions for each molecule. Gaussian fits to each distribution are included for visualization of the data set.

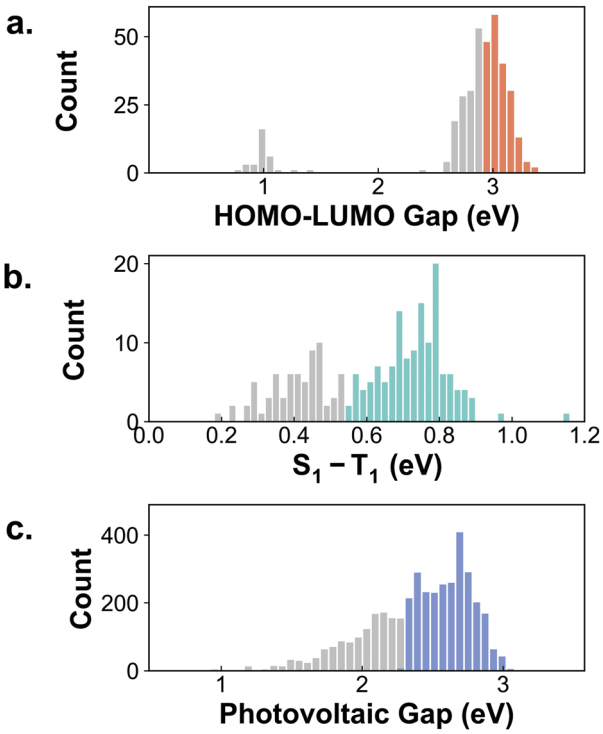


Fig. 3 Individual molecule and donor acceptor pairing screening conditions. (a) HOMO LUMO gap (band gap) of individual molecules, with cutoff value of greater than 2.9 eV highlighted in orange. (b) Calculated difference in individual molecule $S_1$ and $T_1$ splitting energies following HOMO LUMO gap screening, with the selected energetic cut off highlighted in green. (c) Calculated $PV_{gap}$ of viable donor acceptor pairings with cut off of 2.3 eV highlighted in blue.

After employing the steps described above for reducing the possible candidate molecules based on their bandgaps and excited state transition energies, we paired the remaining compounds and compared their HOMO–HOMO and LUMO–LUMO offsets based on their calculated frontier orbital energies. We identified 5151 potential DA pairs, and then tested each pair to see if they could form a viable organic heterojunction, with at least 0.2 eV HOMO–HOMO and LUMO–LUMO offsets. We chose this value as our cutoff because 0.2 eV is the minimum energy offset needed for efficient exciton dissociation at the donor acceptor interface.[30] Imposing this criterion in the energy offset reduced the possible DA pairings from 5151 to 3990 viable pairs. We tested the use of 0.3 and 0.4 eV as offsets instead of 0.2 eV, which further narrowed the number of viable pairings at this stage, but ultimately did not change the final molecules selected through the remaining screening steps. We also mandated a photovoltaic gap ($PV_{gap}$), or the gap between the HOMO of the donor and LUMO of the acceptor, of 2.3 eV in step 4 of the process, as the $PV_{gap}$ relates to the $V_{OC}$ of an OPV comprising the materials pair of interest. With a minimum $PV_{gap}$ of 2.3 eV (Fig. 3c), and accounting for photon energy losses which can be on the order of 0.5–0.6 eV, but have also been reported on the order of 0.3 eV in organic materials,[51,52] we expected the best devices comprising the corresponding donor–acceptor pair to exhibit a $V_{OC}$ of

approximately 2 V. Imposing this cutoff on $PV_{gap}$ screened out approximately one third of the viable DA pairings to 2,661, as highlighted in Fig. 3c. As a result of carrying out steps 1–4, we screened for materials with the most donor-like and acceptor-like character, or equivalently, those at the tails of the HOMO and LUMO distributions shown in Fig. 2a.

Of the 2661 DA pairings that meet the criteria detailed above, we found 88 unique donors and 93 unique acceptors. To further reduce the number of molecules to be screened experimentally, we considered the frequency with which each unique compound was involved in successful pairings by ranking each compound according to the number of pairings it was involved in. We chose to use this criterion to select candidate compounds to synthesize and characterize because we rationalize that this criterion would lead us to donor compounds that are more likely to satisfy our target application. This decision led us to the three molecules shown in Fig. 1: cTBC, cPBC, cTBFBC. The synthesis of these compounds is detailed in the ESI,† and closely follows prior precedent.‡ We were able to grow single crystals of cTBFBC *via* physical-vapor transport that adopt a *C*2/*c* space group, and a new polymorph of cPBC from solution that adopts the *Ima*2 space group. Both structures are included in the ESI.†

To measure the HOMO and LUMO energy levels of these materials and compare the measured values with calculated ones, ultraviolet photoelectron (UPS) and inverse (IPES) spectroscopy were used with energy resolutions of 150 and 400 meV, respectively. The results of these measurements are shown in Fig. 4 and summarized in Table 1. We also compared the electronic properties of these new donors with those of cHBC and cTBFDBC, coronene derivatives that had been extensively studied in OFETs and as donors in OPVs.[46,47,53] We found the experimentally determined HOMO and LUMO energy levels to largely agree with the DFT-calculated values, with a maximum difference of 0.3 eV in the HOMO energy level of cTBC.

To further characterize the new donor materials, as well as to explore and compare the energies of the $S_0 \rightarrow S_1$ and $S_0 \rightarrow T_1$ transitions, we conducted UV-visible (UV-vis) absorption and low-temperature photoluminescence (PL) spectroscopies. Both solution UV-vis and low-temperature PL spectra for each compound are shown in Fig. S3–S7 (ESI†), in which the lowest energy features for both measurements are highlighted with a linear fit and extracted to the point of intersection at the baseline.

For all materials tested in this study, the excited state energies obtained from the onset of the lowest energy absorption of the corresponding PL spectra are summarized in Table 2; the spectra of the individual compounds are shown in Fig. S3a–S7a (ESI†). In Fig. 5a, we highlight the comparison of the predicted and measured values for cTBC; the experimental values and calculated values for the $S_0 \rightarrow S_1$ and $S_0 \rightarrow T_1$ transitions agree within error. We compared the predicted and experimentally obtained

‡ At the time of synthesis, these compounds were new; there have since been reports of their single crystals and their use in transistors, though their energy levels were not characterized *via* USPS/IPES, neither were they incorporated in solar cells.

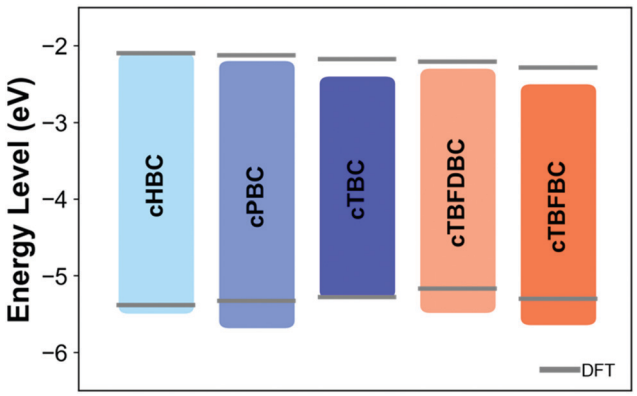


Fig. 4 Comparison of HOMO and LUMO values, as measured by UPS/IPES (colored boxes), and as calculated and calibrated *via* DFT (grey).

Table 1 Summary of calculated and experimental HOMO and LUMO energy levels and the resulting HOMO LUMO gap (band gap), $E_G$

| | Calculated | | | UPS/IPES | | |
|---|---|---|---|---|---|---|
| Material | HOMO (eV) | LUMO (eV) | $E_G$ (eV) | HOMO (eV) | LUMO (eV) | $E_G$ (eV) |
| cHBC | −5.4 | −2.1 | 3.3 | −5.4 | −2.2 | 3.2 |
| cPBC | −5.3 | −2.1 | 3.2 | −5.6 | −2.3 | 3.3 |
| cTBC | −5.3 | −2.2 | 3.1 | −5.2 | −2.5 | 2.7 |
| cTBFDBC | −5.2 | −2.2 | 3.0 | −5.4 | −2.4 | 3.0 |
| cTBFBC | −5.3 | −2.3 | 3.0 | −5.6 | −2.6 | 3.0 |

Table 2 Summary of calculated and experimental $S_0 \rightarrow S_1$ and $S_0 \rightarrow T_n$

| | Calculated | | | Measured | |
|---|---|---|---|---|---|
| Material | $S_0 \rightarrow S_1$ (eV) | $S_0 \rightarrow T_1$ (eV) | $S_0 \rightarrow T_2$ (eV) | $S_0 \rightarrow S_1$ (eV) | $S_0 \rightarrow T_n$ (eV) |
| cHBC | 2.65 | 1.85 | 2.46 | 2.64 | 1.77 |
| cPBC | 2.69 | 1.82 | 2.23 | 2.64 | 1.75 |
| cTBC | 2.69 | 1.84 | 2.69 | 2.65 | 1.83 |
| cTBFDBC | 2.52 | 1.92 | 2.22 | 2.37 | 1.97 |
| cTBFBC | 2.56 | 2.03 | 2.23 | 2.40 | 2.04 |

excited state energies for all five compounds in Fig. 5b and c, respectively. For the phenyl substituted derivatives – cHBC, cPBC and cTBC – we found the calculations to accurately predict both the singlet and triplet splitting energies. On average, the lowest energy triplet state in the phenyl derivatives lies approximately 0.8–0.9 eV below the corresponding singlet state. The invariance of the $S_1 \rightarrow T_1$ splitting energies in these derivatives suggests that the excited state transitions are relatively insensitive to the removal of peripheral benzyl groups.

The experimentally determined excited state energies for the benzofuranyl derivatives cTBFDBC and cTBFBC agree well for the triplet states but show slight deviations for the singlet state. Experimentally, we found the $S_1 \rightarrow T_n$ splitting energies for cTBFDBC and cTBFBC to be approximately 0.4 eV, which is nearly half that of the $S_1 \rightarrow T_n$ transition in cHBC, cPBC and cTBC and falls below the cut-off value set in the screening procedure. Again, as with the phenyl substituted derivatives, we

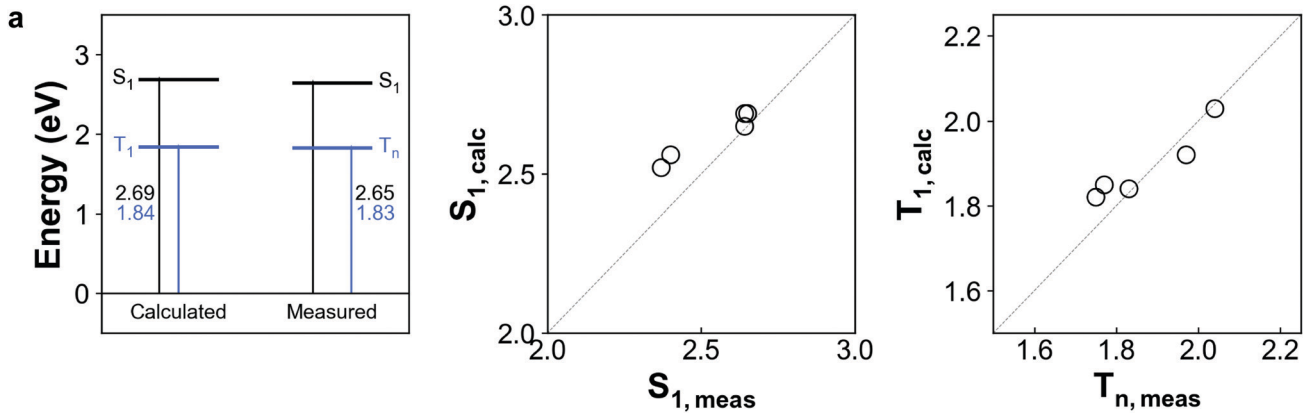


Fig. 5 Comparison of measured and calculated $S_0$ $S_1$ (black) and $S_0$ $T_{1/n}$ (blue) transitions. (a) Transition energies for cTBC as calculated, left, and measured *via* UV Vis and low temperature PL, right. (b) Comparison of $S_0$ $S_1$ transition energies for the selected molecules in this study. (c) Comparison of $S_0$ $T_{1/n}$ transition energies for the selected molecules in this study. Line with unity slope shown in grey for both (b) and (c).

found the removal of one phenyl peripheral group from cTBFDBC to have little impact on the triplet splitting energy. With all derivatives studied herein, the removal of a peripheral phenyl group does not significantly alter the $S_1$ or $T_n$ states for these compounds. We also found the presence of electronegative atoms, such as oxygen in this case, to appear to raise the triplet state, to yield a smaller singlet–triplet splitting energy. We suspect this decrease in the splitting energy to stem from the addition of electron-rich benzofuranyl groups, which have been theorized to have this effect on polycyclic hydrocarbon systems.[54] The implications of modifying these excited states can be leveraged in future materials design for applications, such as organic light-emitting diodes (OLEDs) that rely on thermally activated delayed fluorescence (TADF), through nearly-degenerate triplet states, to improve their efficiencies.[55] Upon finding the electronic properties of these compounds to be largely consistent with calculations, we tested the viability of these materials as active layers in OPVs.

We chose to fabricate and test OPVs with active layers formed by pairing each of the candidate donor compounds with chlorinated contorted hexabenzocoronene derivatives as acceptors.[45,48] In particular, we selected 4Cl-, 8Cl- and 12Cl-cHBC as acceptors as they resulted in DA pairs with properties that met our screening criteria. Further, the HOMO and LUMO energies of these acceptors shift away from vacuum by approximately 1 eV across the series with increasing chlorination, which allows us to systematically assess the ability of our target donor compounds to form organic heterojunctions with acceptors having a range of orbital energies. A summary of each of the resulting device characteristics for each of the donors with each chlorinated acceptor can be found in Table 3 and all OPV device *JV* curves are included in Fig. S8 (ESI†).

Table 3 *JV* characteristics summary

| Donor | Acceptor | $V_{OC}$ (V) | $J_{sc}$ (mA/cm$^2$) | FF | PCE (%) |
|---|---|---|---|---|---|
| cHBC | 4Cl cHBC | 1.80 ± 0.03 | 0.09 ± 0.02 | 0.18 ± 0.01 | 0.03 ± 0.01 |
| | 8Cl cHBC | 1.80 ± 0.01 | 0.3 ± 0.1 | 0.25 ± 0.01 | 0.2 ± 0.1 |
| | 12Cl cHBC | 1.72 ± 0.01 | 0.5 ± 0.1 | 0.43 ± 0.01 | 0.4 ± 0.1 |
| cPBC | 4Cl cHBC | 1.90 ± 0.01 | 0.46 ± 0.01 | 0.30 ± 0.04 | 0.26 ± 0.01 |
| | 8Cl cHBC | 1.75 ± 0.01 | 0.55 ± 0.01 | 0.53 ± 0.01 | 0.51 ± 0.01 |
| | 12Cl cHBC | 1.59 ± 0.01 | 0.47 ± 0.03 | 0.38 ± 0.03 | 0.28 ± 0.04 |
| cTBC | 4Cl cHBC | 1.84 ± 0.01 | 0.52 ± 0.01 | 0.55 ± 0.01 | 0.52 ± 0.01 |
| | 8Cl cHBC | 1.65 ± 0.02 | 0.41 ± 0.01 | 0.49 ± 0.03 | 0.33 ± 0.03 |
| | 12Cl cHBC | 1.70 ± 0.02 | 0.27 ± 0.01 | 0.35 ± 0.01 | 0.16 ± 0.01 |
| cTBFBC | 4Cl cHBC | 1.76 ± 0.01 | 0.6 ± 0.1 | 0.31 ± 0.01 | 0.33 ± 0.01 |
| | 8Cl cHBC | 1.57 ± 0.01 | 0.8 ± 0.1 | 0.60 ± 0.01 | 0.7 ± 0.1 |
| | 12Cl cHBC | 1.43 ± 0.01 | 1.1 ± 0.1 | 0.60 ± 0.01 | 1.0 ± 0.1 |

Our champion device comprises an active layer of cTBC and 4Cl-cHBC in a planar junction architecture. It exhibits a $V_{OC}$ of 1.84 V, a fill factor of 55%, and $J_{sc}$ of 0.52 mA cm$^{-2}$, as shown in Fig. 6b. The active layer also has an average visible transmittance (AVT) of 88%, as shown in Fig. 6c. Compared to previously reported coronene-based OPVs, which comprise an active layer of cTBFDBC and 8Cl-cHBC, the cTBC/4Cl-cHBC device exhibits a $V_{OC}$ that is 0.21 V higher and a 5% improvement in its absolute AVT, from 83% to 88%. This finding is exciting because the resulting device achieves a higher $V_{OC}$ and features an active layer with increased AVT, while maintaining a device FF in line with previous coronene devices. The increase in transparency in these coronene-based active layers arises from changes in the absorption spectrum of cTBC relative to that of cTBFDBC, in which the highest wavelength absorption feature is blue-shifted by 70 nm in the spectrum of cTBC, as shown in Fig. S9 (ESI†). The shift in the absorption onset of the active layer materials does result in a decrease in the device $J_{sc}$ and PCE, relative to previous coronene-based devices due to limited absorption of the solar spectrum. While this trend is expected, we are currently developing algorithms based on optical simulations of optimal devices to identify appropriate optoelectronic properties; coupled with the calculations detailed here, this information can guide the identification of new compounds that can lead to devices with high $V_{OC}$ without necessarily cannibalizing $J_{sc}$.

Further, 9 of the 12 DA pairings tested produced devices with $V_{OC}$s that exceeded the previous record $V_{OC}$ for coronene-based cells. Interestingly, in certain devices and active layers, we find smaller differences between the calculated $PV_{gap}$ and measured

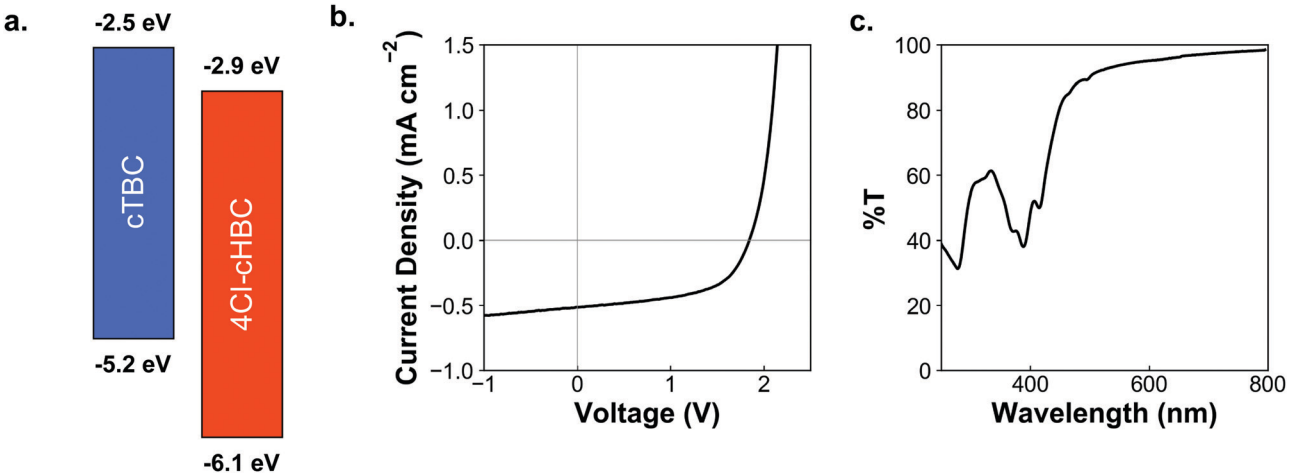


Fig. 6 Solar cell characterization of optimized donor/acceptor pairing as learned from screening set. (a) Energy levels of active layer materials, as measured *via* UPS/IPES, with cTBC as the donor and 4Cl cHBC as the acceptor. (b) *JV* curve of a bilayer OPV. Device characteristics are summarized in Table 3. (c) % *T* of active layer, with resulting AVT of 87.5% for the active layer alone.

device $V_{OC}$, suggesting certain material pairs result in active layers and devices with lower energetic losses. This could stem from factors such as improved charge extraction at interfaces or enhanced charge transport properties in the materials.

In fact, upon comparison of differences between the $PV_{gap}$ of each DA pair and the measured device $V_{OC}$, we found that devices that use cHBC, cPBC, or cTBFBC all feature $V_{OC}$s approximately 0.7 V lower than the $PV_{gap}$, while devices with cTBC as the donor experience much smaller differences, on average only 0.3 V below the calculated $PV_{gap}$. This difference is especially evident in the case of the cTBC/4Cl-cHBC active layer, which relative to a pairing such as cHBC/4Cl-cHBC, with similar or larger energy level offsets, produces devices with a higher $V_{OC}$ and significantly improved fill factor relative to all other devices tested here. Several photophysical considerations are likely at play in this system, such as the position of the triplet states in both materials relative to the charge transfer complex, and further investigation into these phenomena will be the subject of future work.

## Conclusions

In this work, we screened for materials that met our target application, herein transparent OPVs, by employing a series of calculations of pertinent values and then screening the calculations to find materials that satisfy criteria specified to achieve the target application. We considered over 360 possible coronene based molecules in this study, and selected target compounds through a screening procedure. These compounds were then synthesized and characterized experimentally, from which we found good agreement between calculated and experimental orbital and transition energies. Using the donor molecules synthesized, OPVs were tested using halogenated coronene derivatives as acceptors, and the device containing cTBC and 4Cl-cHBC as an active layer produced a $V_{OC}$ of 1.84 V with an average visible transparency of 88%. Both its transparency and open-circuit voltage surpass those of prior coronene based OPVs.

Future work on screening procedures will ideally expand to inform materials development for other applications, such as OLEDs that exploit the TADF phenomenon and would benefit from accurate prediction of singlet–triplet splitting energy. The development of a successful screening procedure for small molecule derivatives with a targeted application provides an example of how computationally aided inverse materials design can drastically accelerate materials development and discovery.

## Conflicts of interest

There are no conflicts to declare.

## Acknowledgements

JCS and Y-LL acknowledge National Science Foundation (NSF) funding under awards CMMI-1824674, DMR-1627453 and DMR-1420541, the latter of which originates from NSF's MRSEC program that supports the Princeton Center for Complex Materials. P. F. has received funding from the European Union's Horizon 2020 Research and Innovation Programme under the Marie Sklodowska-Curie grant agreement no. 795206. HLS and AK acknowledge funding by the NSF under award DMR-1807797, and by a National Science Foundation Graduate Research Fellowship (DGE-1656466) (HLS). SL acknowledges the Department of Energy EERE Postdoctoral Fellowship (Solar Energy). A. A.-G. acknowledges generous support from the Canada 150 Research Chairs Program as well as Dr Anders G. Frøseth.

## Notes and references

1 J. Roncali, P. Leriche and P. Blanchard, *Adv. Mater.*, 2014, **26**, 3821–3838.
2 E. Kim and S. B. Park, *Chem. – Asian J.*, 2009, **4**, 1646–1658.

3 J. A. Gan, Q. L. Song, X. Y. Hou, K. Chen and H. Tian, *J. Photochem. Photobiol., A*, 2004, **162**, 399–406.
4 K. E. Linton, A. L. Fisher, C. Pearson, M. A. Fox, L. O. Pålsson, M. R. Bryce and M. C. Petty, *J. Mater. Chem.*, 2012, **22**, 11816–11825.
5 Z. Yan, Y. Wang, J. Ding, Y. Wang and L. Wang, *ACS Appl. Mater. Interfaces*, 2018, **10**, 1888–1896.
6 T. Lei, J. Y. Wang and J. Pei, *Chem. Mater.*, 2014, **26**, 594–603.
7 S. Himmelberger, D. T. Duong, J. E. Northrup, J. Rivnay, F. P. V. Koch, B. S. Beckingham, N. Stingelin, R. A. Segalman, S. C. B. Mannsfeld and A. Salleo, *Adv. Funct. Mater.*, 2015, **25**, 2616–2624.
8 T. He, M. Stolte and F. Würthner, *Adv. Mater.*, 2013, **25**, 6951–6955.
9 G. L. Schulz, F. S. U. Fischer, D. Trefz, A. Melnyk, A. Hamidi-Sakr, M. Brinkmann, D. Andrienko and S. Ludwigs, *Macromolecules*, 2017, **50**, 1402–1414.
10 M. Cai, X. Bao, X. Wang, H. Zhang, M. Qiu, R. Yang, C. Yang and X. Wan, *Chem. Mater.*, 2016, **28**, 6196–6206.
11 J. Zhang, H. S. Tan, X. Guo, A. Facchetti and H. Yan, *Nat. Energy*, 2018, **3**, 720–731.
12 S. J. Kang, S. Ahn, J. B. Kim, C. Schenck, A. M. Hiszpanski, S. Oh, T. Schiros, Y.-L. Loo and C. Nuckolls, *J. Am. Chem. Soc.*, 2013, **135**, 2207–2212.
13 C. Y. Chiu, B. Kim, A. A. Gorodetsky, W. Sattler, S. Wei, A. Sattler, M. Steigerwald and C. Nuckolls, *Chem. Sci.*, 2011, **2**, 1480–1486.
14 A. Aspuru-Guzik and K. Persson, *Materials Acceleration Platform: Accelerating Advanced Energy Materials Discovery by Integrating High-Throughput Methods and Artificial Intelligence*, 2018.
15 B. Sanchez-Lengeling and A. Aspuru-Guzik, *Science*, 2018, **361**, 360–365.
16 J. P. Correa-Baena, K. Hippalgaonkar, J. van Duren, S. Jaffer, V. R. Chandrasekhar, V. Stevanovic, C. Wadia, S. Guha and T. Buonassisi, *Joule*, 2018, **2**, 1410–1420.
17 P. Friederich, A. Fediai, S. Kaiser, M. Konrad, N. Jung and W. Wenzel, *Adv. Mater.*, 2019, **31**, 1808256.
18 J. J. de Pablo, N. E. Jackson, M. A. Webb, L.-Q. Chen, J. E. Moore, D. Morgan, R. Jacobs, T. Pollock, D. G. Schlom, E. S. Toberer, J. Analytis, I. Dabo, D. M. DeLongchamp, G. A. Fiete, G. M. Grason, G. Hautier, Y. Mo, K. Rajan, E. J. Reed, E. Rodriguez, V. Stevanovic, J. Suntivich, K. Thornton and J.-C. Zhao, *npj Comput. Mater.*, 2019, **5**, 41.
19 E. Soedarmadji, H. S. Stein, S. K. Suram, D. Guevarra and J. M. Gregoire, *npj Comput. Mater.*, 2019, **5**, 79.
20 G. H. Gu, J. Noh, I. Kim and Y. Jung, *J. Mater. Chem. A*, 2019, **7**, 17096–17117.
21 J. J. De Pablo, B. Jones, C. L. Kovacs, V. Ozolins and A. P. Ramirez, *Curr. Opin. Solid State Mater. Sci.*, 2014, **18**, 99–117.
22 J. Hachmann, R. Olivares-Amaya, S. Atahan-Evrenk, C. Amador-Bedolla, R. S. Sánchez-Carrera, A. Gold-Parker, L. Vogt, A. M. Brockway and A. Aspuru-Guzik, *J. Phys. Chem. Lett.*, 2011, **2**, 2241–2251.
23 C. Kuhn and D. N. Beratan, *J. Phys. Chem.*, 1996, **100**, 10595–10599.
24 A. Zunger, *Nat. Rev. Chem.*, 2018, **2**, 0121.
25 A. N. Sokolov, S. Atahan-Evrenk, R. Mondal, H. B. Akkerman, R. S. Sánchez-Carrera, S. Granados-Focil, J. Schrier, S. C. B. Mannsfeld, A. P. Zoombelt, Z. Bao and A. Aspuru-Guzik, *Nat. Commun.*, 2011, **2**, 1–8.
26 L. Fang, P. Liu, B. R. Sveinbjornsson, S. Atahan-Evrenk, K. Vandewal, S. Osuna, G. Jiménez-Osés, S. Shrestha, G. Giri, P. Wei, A. Salleo, A. Aspuru-Guzik, R. H. Grubbs, K. N. Houk and Z. Bao, *J. Mater. Chem. C*, 2013, **1**, 5747–5755.
27 K. Hatakeyama-Sato, T. Tezuka, Y. Nishikitani, H. Nishide and K. Oyaizu, *Chem. Lett.*, 2019, **48**, 130–132.
28 A. M. Chang, B. Rudshteyn, I. Warnke and V. S. Batista, *Inorg. Chem.*, 2018, **57**, 15474–15480.
29 N. C. Davy, M. Sezen-Edmonds, J. Gao, X. Lin, A. Liu, N. Yao, A. Kahn and Y.-L. Loo, *Nat. Energy*, 2017, **2**, 17104.
30 W. Yang, Y. Yao, P. Guo, H. Sun and Y. Luo, *Phys. Chem. Chem. Phys.*, 2018, **20**, 29866–29875.
31 M. Bourass, A. T. Benjelloun, M. Benzakour, M. Mcharfi, M. Hamidi, S. M. Bouzzine and M. Bouachrine, *Chem. Cent. J.*, 2016, **10**, 67.
32 R. Rakhi and C. H. Suresh, *Phys. Chem. Chem. Phys.*, 2016, **18**, 24631–24641.
33 P. Ye, Y. Chen, J. Wu, X. Wu, S. Yu, W. Xing, Q. Liu, X. Jia, A. Peng and H. Huang, *J. Mater. Chem. C*, 2017, **5**, 12591–12596.
34 A. K. Narsaria, J. Poater, C. Fonseca Guerra, A. W. Ehlers, K. Lammertsma and F. M. Bickelhaupt, *J. Comput. Chem.*, 2018, **39**, 2690–2696.
35 W. Saidi, T. Abram, L. Bejjit and M. Bouachrine, *Chem. Methodol.*, 2018, **2**, 247–259.
36 J. W. Patterson, *J. Am. Chem. Soc.*, 1942, **64**, 1485–1486.
37 A. A. Gorodetsky, C. Y. Chiu, T. Schiros, M. Palma, M. Cox, Z. Jia, W. Sattler, I. Kymissis, M. Steigerwald and C. Nuckolls, *Angew. Chem., Int. Ed.*, 2010, **49**, 7909–7912.
38 N. J. Tremblay, A. A. Gorodetsky, M. P. Cox, T. Schiros, B. Kim, R. Steiner, Z. Bullard, A. Sattler, W. Y. So, Y. Itoh, M. F. Toney, H. Ogasawara, A. P. Ramirez, I. Kymissis, M. L. Steigerwald and C. Nuckolls, *ChemPhysChem*, 2010, **11**, 799–803.
39 Y. Zhong, M. T. Trinh, R. Chen, G. E. Purdum, P. P. Khlyabich, M. Sezen, S. Oh, H. Zhu, B. Fowler, B. Zhang, W. Wang, C.-Y. Nam, M. Y. Sfeir, C. T. Black, M. L. Steigerwald, Y.-L. Loo, F. Ng, X.-Y. Zhu and C. Nuckolls, *Nat. Commun.*, 2015, **6**, 8242.
40 Y. Zhong, M. T. Trinh, R. Chen, W. Wang, P. P. Khlyabich, B. Kumar, Q. Xu, C. Y. Nam, M. Y. Sfeir, C. Black, M. L. Steigerwald, Y. L. Loo, S. Xiao, F. Ng, X. Y. Zhu and C. Nuckolls, *J. Am. Chem. Soc.*, 2014, **136**, 15215–15221.
41 Z. Mao, W. Senevirathna, J.-Y. Liao, J. Gu, S. V. Kesava, C. Guo, E. D. Gomez and G. Sauvé, *Adv. Mater.*, 2014, **26**, 6290–6294.
42 S. Rajaram, R. Shivanna, S. K. Kandappa and K. S. Narayan, *J. Phys. Chem. Lett.*, 2012, **3**, 2405–2408.
43 M. Ball, Y. Zhong, Y. Wu, C. Schenck, F. Ng, M. Steigerwald, S. Xiao and C. Nuckolls, *Acc. Chem. Res.*, 2015, **48**, 267–276.

44 Y.-L. Loo, A. M. Hiszpanski, B. Kim, S. Wei, C.-Y. Chiu, M. L. Steigerwald and C. Nuckolls, *Org. Lett.*, 2010, **12**, 4840–4843.

45 A. M. Hiszpanski, J. D. Saathoff, L. Shaw, H. Wang, L. Kraya, F. Lüttich, M. A. Brady, M. L. Chabinyc, A. Kahn, P. Clancy and Y.-L. Loo, *Chem. Mater.*, 2015, **27**, 1892–1900.

46 N. C. Davy, G. Man, R. A. Kerner, M. A. Fusella, G. E. Purdum, M. Sezen-Edmonds, B. P. Rand, A. Kahn and Y.-L. Loo, *Chem. Mater.*, 2016, **28**, 673–681.

47 S. Xiao, M. Myers, Q. Miao, S. Sanaur, K. Pang, M. L. Steigerwald and C. Nuckolls, *Angew. Chem.*, 2005, **117**, 7556–7560.

48 N. C. Davy, M. Koch, G. O. Ngongang Ndjawa, X. Lin, G. J. Man, Y. L. Lin, J. C. Sorli, B. P. Rand, A. Kahn, G. D. Scholes and Y. Loo, *Adv. Energy Mater.*, 2019, **9**, 1901649.

49 Y. Liu, M. Lin and Y. Zhao, *J. Phys. Chem. A*, 2017, **121**, 1145–1152.

50 G. Schwartz, S. Reineke, T. C. Rosenow, K. Walzer and K. Leo, *Adv. Funct. Mater.*, 2009, **19**, 1319–1333.

51 M. C. Scharber, D. Mühlbacher, M. Koppe, P. Denk, C. Waldauf, A. J. Heeger and C. J. Brabec, *Adv. Mater.*, 2006, **18**, 789–794.

52 J. Benduhn, K. Tvingstedt, F. Piersimoni, S. Ullbrich, Y. Fan, M. Tropiano, K. A. McGarry, O. Zeika, M. K. Riede, C. J. Douglas, S. Barlow, S. R. Marder, D. Neher, D. Spoltore and K. Vandewal, *Nat. Energy*, 2017, **2**, 17053.

53 A. M. Hiszpanski, S. S. Lee, H. Wang, A. R. Woll, C. Nuckolls and Y.-L. Loo, *ACS Nano*, 2012, **7**, 294–300.

54 S. Escayola, M. Callís, A. Poater and M. Solà, *ACS Omega*, 2019, **4**, 10845–10853.

55 X. K. Chen, D. Kim and J. L. Brédas, *Acc. Chem. Res.*, 2018, **51**, 2215–2224.